A study on giant radio pulses

Karuppusamy, R.

CHAPTER 5

Crab Giant Pulses at Low Sky Frequencies

R. Karuppusamy and B. W. Stappers

To be submitted, Astronomy & Astrophysics

Abstract We collect and analyse a large number of Crab giant pulses at very low sky frequencies in the 115–180 MHz range, using a baseband recorder and full coherent dedispersion. From the dispersion-free giant pulses, we derive the scatter timescales and the pulsar spectrum in this frequency range. Our sensitive observations and coherent dedispersion shows that there is a precursor to the interpulse and that it comprises no giant pulses and so can be attributed to a similar emission source as the precursor to the main pulse. Together these precursors might be the normal emission seen from the majority of radio pulsars. More than 1000 giant pulses are detected at each of the frequencies observed. From this the giant pulse emission rates are found and the scatter timescales are computed in each observed band.

5.1 Introduction

The Crab nebula and pulsar are amongst the most intensively studied objects on the sky. The discovery of the pulsar NP 0531 (now known as PSR B0531+21) in the Crab nebula (also designated as SN 1054) was the first observational evidence for neutron stars being formed in the supernova explosion of massive stars (Staelin & Reifenstein 1968). The Crab pulsar is a bright source of electromagnetic radiation and is detected at all observable wavelengths. At radio frequencies, the pulsar emission shows a variety of features of which the evolution of the average pulse profile with increasing sky frequency is readily noticed. For example, in addition to the main and inter pulse emission visible at most frequencies, other emission components appear at certain frequencies; the precursor emission component is visibile only at very low frequencies (Rankin et al. 1970); the low-frequency component appear between 600–4800 MHz and two high-frequency components in the 4000–8400 MHz frequency range (Moffett, D. A. and Hankins, T. H. 1996). In the latter work, it is also seen that no interpulse emission is present at 2700 MHz, and reappears slightly earlier in phase above 4700 MHz. The most enigmatic feature in the radio emission from the pulsar is the intense radio bursts called giant pulses, which actually led to the discovery of the Crab pulsar (Staelin & Reifenstein 1968). The giant pulses were reported for the first time by Sutton et al. (1971) as "jumbo" pulses that formed a long tail in the single pulse intensity histogram. Soon after this work, the individual pulses from the Crab pulsar were extensively characterised and the power-law nature of the pulse energy distribution was firmly estalished (Argyle & Gower 1972; Gower & Argyle 1972).

Giant pulses are now defined as the pulses with energy greater than ten times the average pulse energy and have widths very narrow compared to the average pulse emission (Knight 2007). As an example, narrow pulses on the order of 0.4 ns are observed at a sky frequency of 9 GHz (Hankins & Eilek 2007). However, at low sky frequencies, the signal propagation effects in the interstellar medium (ISM) blur the narrow pulse considerably; the dispersion smearing at different frequencies arrive at slightly different times due their travel in the ionized ISM and pulse broadening due to multipath propagation effects (Williamson 1973). In the past studies, either hardware limitations in correcting the dispersion smearing or less sensitive systems limited the number of giant pulses studied at low frequencies. For example, the early studies relied on less than 400 giant pulses (Sutton et al. 1971; Argyle & Gower 1972; Gower & Argyle 1972). More recently Popov et al. (2006b) used a sensitive telescope, but an incoherent dedispersion method and Bhat et al. (2007) coherently dedispersed pulsar signal, but used a less sensitive system. As an illustration, the dispersion smearing in the 2.5 MHz band at our lowest sky frequency, 116.75 MHz is 766.75 ms, which is ~23 pulse periods. Even with a reasonable 64-channel hardware filter bank, the dispersion smearing in each channel is 11.9 ms, which if not removed allows the detection of only the very bright pulses.

The Crab pulsar has a rather steep spectrum of $\alpha = -3$ (Rankin et al. 1970; Maron et al. 2000). This implies that a large number of giant pulses should be detectable at low sky frequencies, if their occurance rate remains the same as that reported at higher frequencies (Lundgren et al. 1995). Scattering affects normal pulses and giant pulses alike, but the effect

is more readily measured in the giant pulses. If the dispersion smearing can be fully removed, the giant pulse emission rates and the scattering phenomena can be studied in much greater detail. The observing system we use has the possibility to coherently dedisperse the pulsar signal. Thus this study marks the first coherently dedispersed study of the emission from the Crab pulsar with a resonably senstive system, resulting in a large number of giant pulses in the frequency range 115–180 MHz. The preceeding discussion motivates revisiting the giant pulse emission at low sky frequencies.

The rest of the chapter is organised as follows: The observations are described in §5.2. The flux calibration, average radio emission and the spectra of the Crab pulsar are discussed in §5.3. The single pulse statistics are discussed in §5.4. Scattering in single pulses across the range of observed frequencies is presented in §5.5, followed by discussion and conclusions.

5.2 Observations and data reduction

For the observations reported in this chapter, we used the flexible baseband recording and processing instrument, PuMa-II (Chapter 2) and the Low Frequency Front Ends (LFFEs) at the Westerbork Synthesis Radio Telescope (WSRT). The LFFEs were tuned to eight frequencies each of which was 2.5 MHz wide in the 115–180 MHz frequency range (details in Table 5.1). The observations were carried out on 2006 May 13, spread over four 15-minute sessions. The baseband recorded pulsar signal was coherently dedispered at the dispersion measure (DM) obtained from the Crab pulsar ephemeris maintained by the Jodrell Bank Observatory[1]. A 32-channel coherent filterbank was formed using the open-source pulsar data processing software package DSPSR[2] and all single pulses were written to disk. The PSRCHIVE (Hotan et al. 2004) software was used to form total intensities and further processing. Single pulses satisfying the threshold $S/N \geq 4.4\sigma$ in total intensity were examined by eye and pulses not contaminated by RFI were retained for the single pulse analysis.

Separate 10-second stretchs of average pulse profiles were also formed using a 64-channel coherent filterbank. The average emission in all four sessions for two frequencies are displayed as a grey scale plot in Figure 5.1. The system was also the most sensitive in sessions II and III, as the sensitivity depends on the hour angle of the Crab pulsar when it was observed (as explained in the next section).

5.3 Low frequency flux

5.3.1 Flux Calibration

The Crab nebula is a bright extended object with a typical size of $6' \times 4'$ and therefore dominates the telescope system temperature when the width of the telescope beam is comparable to the angular size of the nebula. The frequency dependence of the nebular flux can be expressed as $955\nu^{-0.27}$ where ν is the sky frequency in GHz (Bietenholz et al. 1997). For these

[1] http://www.jb.man.ac.uk/ pulsar/crab.html
[2] http://dspsr.sourceforge.net/

Frequency (MHz)	Session I 08:59:50	Session II 11:59:50	Session III 14:59:50	Session IV 17:59:50
116.75	X	X	X	X
122.75	*	*	*	–
139.125	X	X	X	–
141.75	–	–	X	X
147.50	–	X	X	X
157.00	X	X	X	–
162.50	X	X	X	–
173.85	X	X	X	X

Table 5.1: Details of the observations carried out on 13 May 2006. The 15–minute observing sessions began at the start time in UTC, displayed in the second row. The successful runs are marked with the symbol 'X' and failed recording with '–'. The runs with '*' were severely affected by interference and were ignored in the analysis.

observations, the WSRT was configured to operate in the tied array mode, where the signals from fourteen 25-m telescopes were coherently added by special purpose hardware. The resulting synthesised beam depends on the source hour angle and sky frequency; in the 115–180 MHz range the beam resolves the nebula at higher frequencies and at small hour angles of the Crab pulsar. At 116 MHz, the beam is approximately the size of the nebula; the emission from the nebula is therefore unresolved; this further results in a large system temperature and hence a less sensitive system. The resulting pulse intensity variation with respect to observation time is displayed in Figure 5.1 and shows the frequency–time dependence of the beam width.

Observations at low sky frequencies are prone to RFI and the data affected by RFI has to be removed before calibration of the single pulses or the average pulse profile. To clean the data of RFI from the average profiles, the 10 seconds subintegrations were inspected visually as frequency–phase plots and RFI affected data stretchs were removed in this process. The remaining data was integrated to estimate the average pulse fluxes.

From Figure 5.1, a relatively large signal-to-noise ratio is seen in the observing sessions II and III. Therefore, we use the average profiles formed from the observing session III to estimate the average pulse flux. The change in the nebular contribution to the system temperature due to the frequency–time dependence of the beam width was incorporated in the estimation of pulse fluxes in a manner similar to the method described in §3.3. Since the former work was at 1400 MHz, we need to use revised values corresponding to the frequency range considered here. Accordingly, the receiver temperature is taken to be a constant value of 400 K in the 115–180 MHz range of the frontend receivers. The nominal background sky temperature spectrum of $\nu^{-2.6}$ is compensated electronically in the amplitude gains of LFFE amplifiers. To this value, the contribution of the Crab nebula is added to give the system temperature, assuming a 25% aperture efficiency and a telescope gain of 0.57 K Jy^{-1}. The uncertainty in the flux estimates are taken to be 10%, which includes the possible effects due

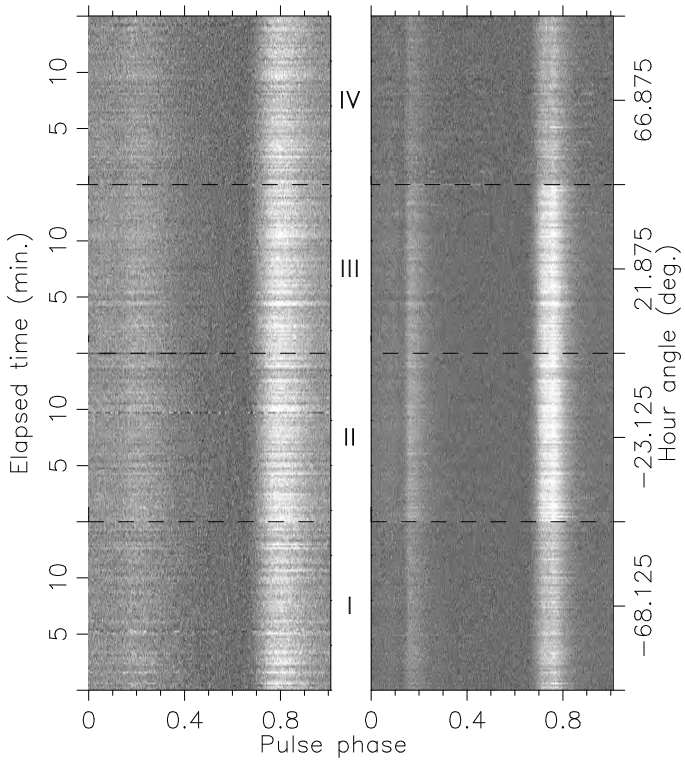

Figure 5.1: Plot of total intensity of Crab pulsar against time in the four observing sessions shown separated by dashed horizontal lines. The left panel corresponds to the band centred at 116.75 MHz, while the panel on the right is at 157 MHz. The elapsed time shown on the vertical axis is the observation time within each session. The vertical axis is labelled with the hour angle of the Crab pulsar on the right side of the second panel and corresponds to the middle of the 15-minute observing sessions.

to the remaining RFI and the uncertainties in the estimation of the Crab nebula's contribution to the system temperature.

5.3.2 Average pulse profiles

Figure 5.2 shows the average pulse profiles at several frequencies observed at the WSRT and the γ-ray profile from Abdo et al. (2009a). It is of interest to note the features in the average emission at the low sky frequencies. The increase in scatter broadening of the pulses is clearly visible as one moves down in frequency. We identify at least four emission components – the precursor to the main pulse, the main and interpulse and the new precursor to the interpulse (see Figure 5.2). A weak emission brigde that appears to connect the main and interpulse appears convolved with the scatter tail of the main pulse. These emission features are discussed below. In the 1400 MHz data, the weak emission that preceeds the main pulse

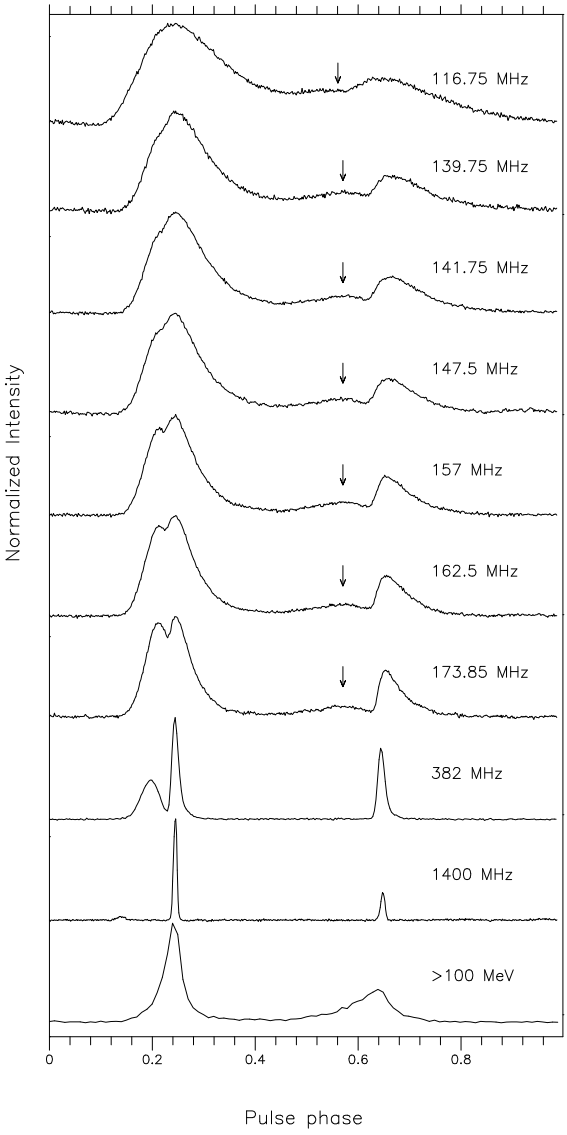

Figure 5.2: Plot showing the average emission profiles of the Crab pulsar at several frequencies observed at the WSRT aligned by the peak in the main pulse. The first seven profiles are from the observations reported in this work, while profiles at 382 MHz and 1400 MHz are from the WSRT archives. The γ–ray profile was provided by the Fermi collabration. The arrow shows the location of new interpulse precursor emission component.

is the low-frequency component (Figure 1; Moffett, D. A. and Hankins, T. H. 1996).

Apart from the scattering, a gradual decrease in the ratio of main pulse to interpulse peak intensity is visible. The emission bridge is convolved with the main pulse scatter tail and it increases towards lower frequencies. At 116.75 MHz the feature is ~ 40% of the peak main pulse intensity. Previous studies have revealed the emission bridge (Rankin et al. 1970; Manchester et al. 1972; Vandenberg et al. 1973), although it was not very evident as the signals were affected by dispersion smearing.

The precursor to the main pulse is not resolved below 147.75 MHz due to scatter broadening while vestiges of it are still visible at 139.75 MHz. The precursor appears marginally weaker in relation to the main pulse for frequencies below 173.85 MHz, while it is fully resolved at 382 MHz, it is absent at 1400 MHz. The low frequency average emission profiles in Figure 5.2 all show indications of a precursor to the interpulse. However, at lower frequencies, this component is completely masked by the long scatter tail of the main pulse. However, the slight increase in emission is clearly visible, as indicated by the small arrow in the figure.

To the best of our knowledge, this is the first instance that the precursor to the interpulse is reported. We now draw comparision to the main pulse counterpart. Both features appears to increase in intensity as we move down in frequency. The new component has no emission counterparts at higher radio frequencies or other wavelengths. This is also true of the main pulse precursor that disappears for frequencies greater than ~600 MHz. Other than the first order comparision, more observations are necessary to ascertain the nature of the new component. For example, the main pulse precursor is linearly polarized (Campbell & Heiles 1970) and its intensity varies in time on the order of a few tens of minutes (Rankin et al. 1970). However, we draw one important conclusion – the new component can be interpreted as comprising of the normal interpulse emission in a similar manner as the main pulse precursor (Popov et al. 2006a) and this is dicussed in §5.6.

The average γ-ray emission is seen only at the phases coincident with the radio giant pulse emission phases, and no other emission component is visible. There are no counterparts to the emission features discussed at very low sky frequencies.

5.3.3 Radio spectrum

The flux calibrated average pulse profiles from the observing session III were used to compute the mean continuum flux density for the Crab pulsar, as this session was the least affected by RFI and has the best S/N of the four obsering sessions. The spectrum is displayed in Figure. 5.3 and is derived from the computed mean flux densitites.

The spectrum displayed here can be compared to Sieber (1973), where the low frequency part of the spectrum in their work was derived from the continuum fluxes. In their work, it is seen that the spectrum turns over at ~100 MHz. In the figure above, the 10% uncertainty in the flux at 116.75 MHz maybe an underestimation, as at this frequency the whole nebula is illuminated by the telescope beam. Therefore, this could be the reason for the somewhat lower measured flux at 116.75 MHz, and the apparent turnover of the spectrum in this frequency range. The table in the work of Manchester et al. (1972) shows that the flux density increased

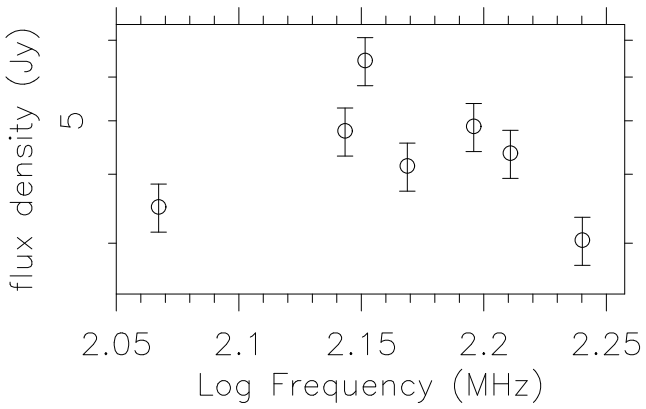

Figure 5.3: The spectrum of the Crab pulsar in the 115–180 MHz range. The error bars correspond to 10% uncertainty in the flux measurements. The observation from Session III was used to derive the flux densities shown here.

down to the lowest frequency they observed. the possiblity of flux underestimation in our 116 MHz data means that we can neither confirm nor contradict the results in the former work.

5.4 Giant Pulse Statistics

In this section, the statistics of the giant pulses are examined by means of the mean flux density distribution of single pulses. We began by searching for the giant pulses based on a threshold of $S/N \geq 4.4\sigma$, where σ is the off-pulse root-mean-square variation of the noise. Furthermore, only pulses that showed proper phase association to the average emission profile were collected. Next, the flux density of single pulses was computed, and then averaged over the pulse period to compute the average flux density of the single pulses. At low sky frequencies the scattered giant pulses can occupy a considerable fraction of the pulse period. For this reason, initially a few giant pulses were examined by eye in every band recorded, from which a window of suitable size was found to include all pulsed emission from the star. After calibrating the pulses, the flux was integrated in this window and divided by the peak value resulting in the equivalent width, W_{eq} of the pulse. The flux of the pulse is then computed using W_{eq} in the radiometer equation (as discussed in Chapter 3) and then averaged over the pulse period.

Subsequently, a second level search was undertaken to locate all broad band pulses. Using the giant pulses at 173.85 MHz and the dispersion delay at other frequencies, simultaneous pulses were recovered. This resulted in pulses at 173.85 MHz and at least one other frequency. From these pulses, of the 172 brightest detected at 173.85 MHz, 16 were detected in all seven bands with $S/N > 15\sigma$. These pulses were therefore very broad band, i.e $\Delta\nu/\nu \sim 0.3$. However, these pulses are only a small fraction of the total number of giant dectected at 173.85 MHz, and in the following we rule out scintillation as a possible cause. The diffractive

scintillation bandwidth, $\Delta\nu_d$ at 430 MHz for the Crab pulsar was found to be 24 KHz (Table 3;Cordes et al. 2004). Using a nominal $\Delta\nu_d \propto \nu^4$ frequency scaling, we expect $\Delta\nu_d$ to be on the order of 0.12–8 KHz and this is much smaller than the 2.5 MHz bandwidth used. Therefore, diffractive scintillation cannot be the cause for fewer broad band giant pulses. Also, refractive interstellar scintillation cannot cause deep modulations across the frequency band observed as the timescales are on the order of a few days (Lundgren et al. 1995).

The number of pulses at the main and inter pulse phases detected in the first pass are shown in Table 5.2. The reason for a larger number of detections in the higher frequency bands is due to the increased sensitivity of the telescope array as discussed earlier in §5.3.1. At 116.75 MHz, a somewhat larger number of pulses were detected owing to the longer observation (see Table 5.1).

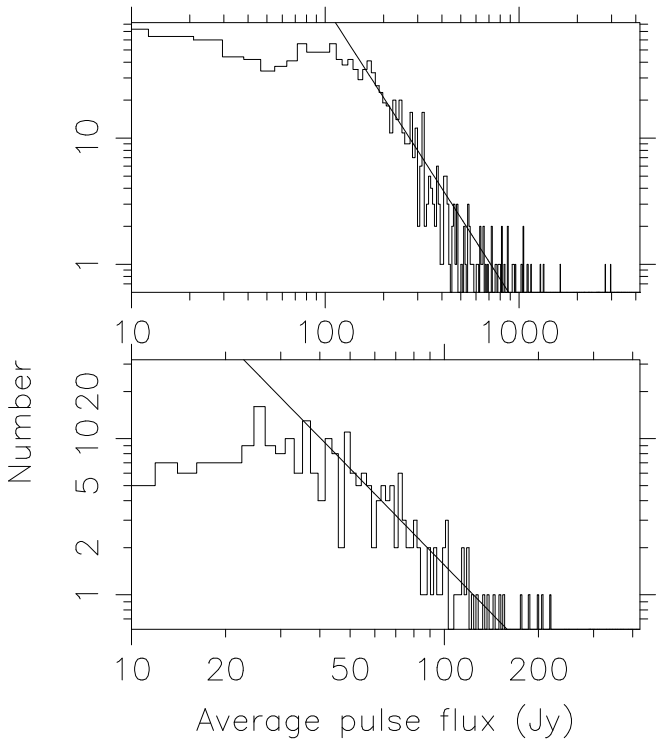

Figure 5.4: Plot showing the distribution of the average flux density for the pulses found at the main and inter pulse phases at the band centred at 173.85 MHz. Giant pulses dectected in other bands show similar a trend. Also shown are the power law fits to the distribution.

Figure 5.4 shows the flux distribution of the giant pulses at 173.85 MHz. The other bands display similar histograms and are therefore not shown. In all bands we note that, the giant pulses are more frequent and bright at the main pulse phase compared to those at the inter pulse phase, and this is entirely consistent with the emission at higher frequencies (Lundgren

et al. 1995). To derive a rate of emission, the probablity density function is modelled as,

$$f(S_\nu) \propto S_\nu^{-\alpha}, \qquad \text{for } S_\nu > S_b \tag{5.1}$$

where S_ν is the mean flux density at frequency ν, and S_b defines the point in the distribution beyond which a power law emerges. Using a similar method and as displayed in Figure 5.4, power-law fits to the pulse flux distributions at other frequencies were made, and the slopes derived are shown in Table 5.2. The slopes of the distributions steepen with frequency except at 116.75 MHz, which is probably due to an uncertainty in estimation of average pulse flux. Additionally, in this band the pulse emission occurs over a large fraction of the pulse period resulting in an insufficient off-pulse region contributing to flux estimation uncertainties. Alternatively, the drastic turn over in the spectra of the pulsar at ∼100 MHz (Rankin et al. 1970 and Figure 5.3 in §5.3.3) might cause a steepening in the distributions.

Frequency	N_{pulses}		α_{mp}	α_{ip}	rate
(MHz)	MP	IP			second^{-1}
116.75	1246	370	2.12±0.09	2.7 ±0.29	14.8×10^{-3}
139.125	581	206	1.65±0.14	1.2 ± 0.13	9.6×10^{-3}
141.75	964	156	1.51± 0.05	1.6 ± 0.09	20.5×10^{-3}
147.50	1047	313	1.78 ± 0.10	1.6 ± 0.12	16.6×10^{-3}
157.00	1175	409	1.83± 0.10	0.7 ± 0.05	19.3×10^{-3}
162.50	1165	-	2.38 ± 0.15	-	14.2×10^{-3}
173.85	1355	330	2.39 ± 0.12	2.05 ± 0.16	15.4×10^{-3}

Table 5.2: The number of giant pulses detected, the slopes of average pulse flux histograms and the giant pulse rate in various bands observed. The number of pulses detected in the bands centred at 139.125 and 141.75 MHz are considerably less than the other bands because only two of the four observing session contained usable data for these two bands. the giant pulse rate included both the inter and main pulse giants.

The slopes to the flux distribututions found here can be compared to those reported elsewhere. Argyle & Gower (1972) report a slope of -2.5 and -2.8 for the main and inter pulse flux distributitons at 146 MHz. These results are based on their 171 pulses in two observations using 46-m and 26-m antennae. The difference in the values we derive are likely due to the small number statistics and limited sensitivity of Argyle & Gower (1972). We can also compare the slopes estimated at other frequencies. From our earlier work at 1400 MHz (Chapter 3), it was shown that the slopes were −3.0 and −2.8 for the main and inter pulses flux distributions, respectively. Lundgren et al. (1995) reported a value of −3.3 at 800 MHz and Cordes et al. (2004) reported ≈ −2.3 at 430 MHz and noted that the slope increased with frequency. Combined with our values at 115–180 MHz, we confirm the general steepening of the flux distrubtions with increasing frequency. The rate of giant pulses is also higher at low frequencies. At 173 MHz, a total of 1685 giant pulses above with $S/N \geq 5.2\sigma$ were detected (see Table 5.2). This translates to a rate of one giant pulse in 62 stellar rotations. The rate

of giant pulse emission (column 7 in Table 5.2) shows no particular trend with frequency. The complex nature of the telescope beam and the presence of any residual RFI might have affected the giant pulse rates derived here.

As reported elsewhere, we confirm that there are no giant pulse emitted at other than the main and inter pulse phases. An extensive search at both the precursor phases resulted in no giant pulse detections. Additionally, we computed the longitude resolved modulation index for the longitude range corresponding to the main pulse precursor, and find a value of ≈ 0.8. The large number of giant pulses at the main and inter pulse phases resulted in strong intensity variations leading to a correspondingly large modulation index of ≈ 3. This supports the argument that the main pulse precursor consists of entirely normal pulses, and hence shows a very small pulse to pulse intensity variation, unlike the emission at the main and inter pulse phases.

5.5 Scattering Analysis

5.5.1 Scatter timescales

The single bright pulses are excellent probes of the scattering interstellar medium. The propagation of the intrinsically narrow pulse through the interstellar medium and the scattering material within the Crab nebula results in the observed exponential tail in the low frequency average profiles and giant pulses. We model the giant pulses as consisting of a Gaussian like leading edge and an exponential decay. This can be written as,

$$f(t) = \begin{cases} A \cdot e^{-\frac{(t-t_m)^2}{2\sigma^2}} & \text{if } t < t_m \\ A \cdot e^{-\frac{t-t_m}{\tau_{sc}}} & \text{if } t \geq t_m. \end{cases} \tag{5.2}$$

where t_m is the time where the exponential decay of the trailing edge begins, σ is the width of the one-sided Gaussian with A as a propotionality constant. The best fit curves to the data based on equation 5.2 is shown in Figure 5.5. The scattering timescales τ_{sc}, are given by the $1/e$ decay times which is estimated from the exponential fits to the trailing part of the giant pulses.

The scattering in the direction of the Crab pulsar is assumed to originate from a single, thin slab of scattering material giving rise to a Kolgomorov spectrum. This results in the frequency scaling of the scattering time as $\nu^{-4.4}$. The average of the derived scatter times from the individual giant pulses in every observed band was computed. Example fits are displayed for seven of the observed bands in Figure. 5.5.

5.5.2 Statistics of scatter timescales

The distribution of the scatter times is displayed in the top panel of Figure 5.6 and corresponds to the band centred at 173.25 MHz. Giant pulses in bands at other frequencies observed here display qualitatively similar histograms. The spread in the histogram is caused by the values from fits to weak pulses, which may have larger errors. The average of the scattering

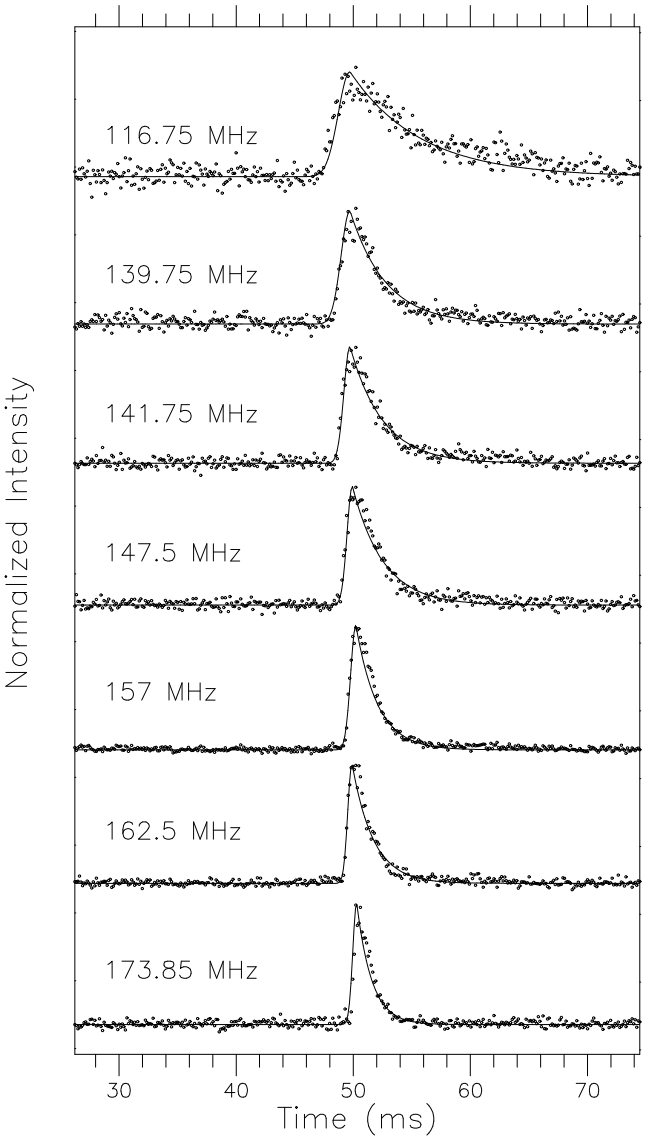

Figure 5.5: Plot displaying a broad band giant pulse detected in seven of the eight recorded bands. The observed total intensity of the pulse is modelled using a functional form described in the text.

timescales was computed at each frequency. These values are plotted and the best fit is shown in the lower panel of Figure 5.6. The spectra of scatter timescales is well-described by a $\tau_{sc} \propto \nu^{-3.2\pm0.08}$ relation. At an epoch only 233 days earlier than our observations, Bhat et al.

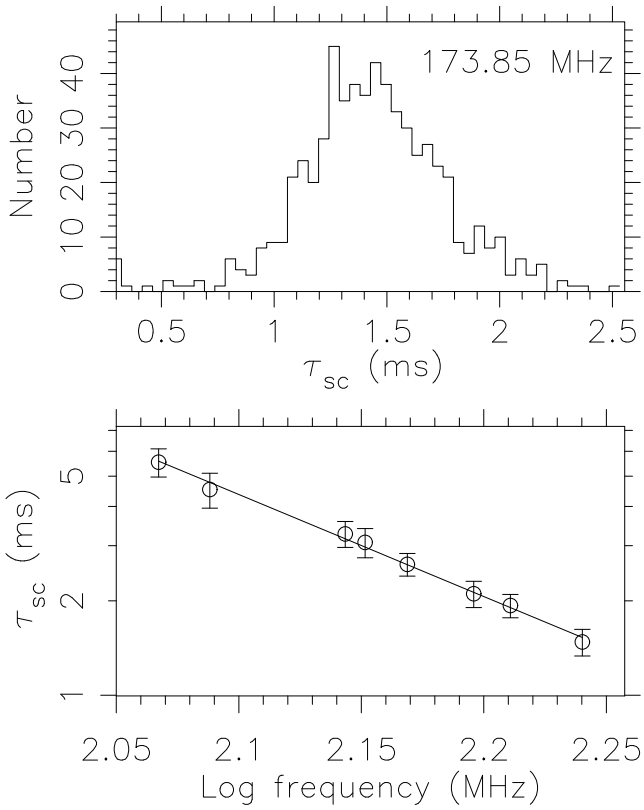

Figure 5.6: Plot showing scatter times from the model fits. The top panel shows the distribution of the scattering timescales in the band centred at 173.85 MHz. The bottom panel shows the average scattering timescales from the other bands.

(2007) derive a frequency scaling of $\nu^{-3.5\pm0.3}$ based on τ_{sc} at several frequencies reported elsewhere and their value at 200 MHz. Therefore, the frequency scaling we derive is in good agreement with that of Bhat et al. (2007). We also note that the Crab nebula shows abnormal scattering events where scattering timescales can drastically change with in a few weeks. The lower index of ~ -3.2 to -3.5 is inconsistent with the expectation of -4.4 for a Kolgomorov spectrum. However, the Kolgomorov spectrum is applicable to the distributed interstellar medium, while most of the scattering in the pulses from Crab pulsar orginates within the nebula.

5.6 Discussion and conclusion

The simultaneous average emission profiles at several frequencies in the 115-180 MHz range are reported for the first time. From the coherently dedispersed signal, we report the previously unidentified interpulse precursor and we compared it to the main pulse precursor. Popov et al. (2006a) hypothesise the latter emission component as consisting of normal pulses from the pulsar, and that the conventional main pulse is made of entirely giant pulses. Their arguments were based on the finding that the average profile formed using only giant pulses has a remarkable similarity to the average emission profile at that frequency and that the phase of giant pulses trail the average emission in certain pulsars like PSR 1937+21 (Kinkhabwala & Thorsett 2000). This interpretation was supported by the high-energy emission occuring coincient with the phase of the giant pulses as seen in PSRs B1937+21 (Cusumano et al. 2003), B1821-24 (Romani & Johnston 2001) and the Crab pulsar (Figure 5.2). The forgoing discussion and our finding of the new interpulse precursor supports the view of Popov et al. (2006a) where the conventional main and interpulse emission consists only of giant pulse emission.

The new emission component can be robustly tested by means of a simulation and will be done in our future work. This can be done, for example, by assuming a xe^{-x} functional form of the scattering effects, and a narrow pulse representing the pulse emitted at the source. A model with interpulse precursor emission component was tested in the work of Manchester et al. (1972), and this template was smoothed using functions that represent both dispersive and scattering effects. With our observations, the dispersive effects are completely removed, and only effects of scattering needs to be tested. Combined with observations at other sky frequencies, we further confirm that the main and inter pulse precursor components have very steep spectral indicies. Moreover, these component have no counter parts at other wavelengths. The radio spectrum of the Crab pulsar we derive is qualitatatively consistent with spectra published in earlier works.

The Crab giant pulse emission is limited to the main and interpulse phases at this frequency, as reported in past studies. The phase of the main and inter pulses has counter parts at the γ-ray wavelengths. The enhanced emission at optical wavelengths coincident with the giant pulses reported by Shearer et al. (2003) may be true at the γ-ray wavelengths too. This hypothesis was tested by Lundgren et al. (1995) and they found no correlation between γ-ray and giant pulse emission at 800 MHz. However, this can now be tested at a higher significance with the Fermi telescope and to much higher photon energies. There has been one reported detection of giant pulse emission at the so-called high frequency component (Jessner et al. 2005), at a sky frequency of 8.35 GHz. Even though we detect the precursor component with a large S/N, we confirm that no giant pulses are dectected in the longitude corresponding to the precursor. A low value of modulation index at the precursor phase is further evidence that the giant pulses donot occur at this frequency or have a extremely low occurance rate.

The finding of some giant pulses with $\Delta\nu/\nu \approx 0.3$ suggests that the giant pulse emission can be very broad band at low frequencies. This value is higher than the value of ~ 0.1 as found in Chapter 3 for frequencies of $\sim$1400 MHz. We note that only a small fraction of the giant pulses show such broadband emission at these frequencies in contrast to the vast

majority of the pulses. From the general increase of the slopes of pulse flux distributions with frequency, it is clear that the giant pulses are more frequent at lower sky frequencies. Simultaneous multifrequency observations and similar data reduction and analysis techniques used in this chapter might help resolve the true emission bandwidths of giant pulses.

We have probed the propagation effects in the interstellar medium and the Crab nebula in the 115-175 MHz range from the scatter tails of the giant pulses. Complete removal of dispersion smearing allowed a greater experimental precision in the determination of scattering timescales than the previous studies. For the epoch of the observations reported here, the scattering time scales in the direction of the Crab nebula follow a $\nu^{-3.2\pm0.08}$ dependence. The different values for the scattering spectra derived by various authors confirms that a single Kolmogrov like spectrum is an insufficient description of the scattering medium. A possible reason for this departure is probably the nebula surrounding the pulsar.

5.7 Acknowledgements

We acknowledge the use of European Pulsar Data network, the ATNF pulsar catalogue and the SAO/NASA Astronomical Data System maintained by Harvard-Smithsonian Center for Astrophysics. The WSRT is operated by ASTRON/NWO. We thank the observers for the system set up prior to the observations. The PuMa-II instrument and RK are funded by Nederlands Onderzoekschool Voor Astronomie (NOVA). RK thanks M. Serylak for discussions and for help in data analysis.